Radar subsurface mapping of the polar layered deposits on Mars

Daniel Cahn Nunes[1] and Roger J. Phillips[2]

Received 17 October 2005; revised 15 February 2006; accepted 27 February 2006; published 8 June 2006.

[1] Determining the three-dimensional (3-D) structure of the Martian polar caps is fundamental to understanding their hydrologic history, dynamic behavior, past climatic changes, and the underlying lithosphere, and radar sounding is the most promising technique to do so. We model the dielectric profile of the Martian polar layered deposits (PLD), apply it to a 1-D electromagnetic plane wave propagation model, and calculate the relative strength of radar reflections produced by layering within these deposits. Variations in dust fraction with depth derive from albedo profiles of a northern polar trough and a radiative transfer model. Detection of the fine-scale layering present in the polar deposits with SHARAD is likely under a wide range of possible dielectric properties of the ice and silicate inclusions as long as minimum inclusion volumetric fractions are larger than 10^{-3}. Our models indicate also that stratigraphic mapping of the PLD is feasible with a vertical resolution of $\sim$20 m under ideal conditions. Penetration depths depend greatly on the dielectric properties of silicate inclusions, reaching at least 250 m for ice rich in highly conductive altered basaltic dust to at least 2 km for weakly conducting silicate inclusions. Because of the wide parameter space and unconstrained composition, interpretation of polar radar data will be best accomplished in conjunction with updated thermal models and other data sets, such as the recently published results from orbital infrared remote sensing that impose limits on ice grain size and dust.

Citation: Nunes, D. C., and R. J. Phillips (2006), Radar subsurface mapping of the polar layered deposits on Mars, *J. Geophys. Res.*, *111*, E06S21, doi:10.1029/2005JE002609.

1. Introduction

[2] The water-rich Martian polar caps and their layered structure are thought to hold crucial information on the climatic history and the hydrologic cycle of Mars [*Laskar et al.*, 2002; *Thomas et al.*, 1992]. A basic understanding of the evolution of the caps, however, is handicapped by our inability to definitively answer several first-order questions, as we lack substantial observational constraints necessary for useful geophysical modeling. Are the caps composed predominantly of water ice, or are other phases such as silicate inclusions, dry ice, and CO_2-clatherates significant components? What is the thermal state of the polar caps, and would it support melting at depth? How is the load imposed by each cap mechanically compensated and to what degree are the caps flowing viscously?

[3] Most of what is known about the caps derives from remote sensing of their upper few meters and observations of their surface, troughs, and scarps. Radar sounding, in contrast, has the capability of providing a three-dimensional view of the polar caps because H_2O and CO_2 ices possess very low electric conductivities and, consequently, only weakly attenuate the propagation of electromagnetic (EM) waves. Mixtures of these ices with generic impurities such as sediment and salts have a wide range in permittivity and conductivity values [e.g., *Ulaby et al.*, 1986]. It is exactly these variations in material electrical properties that a radar sounder might detect in the subsurface, giving us the opportunity of mapping the layered structure of the Martian polar caps, perhaps the presence of meltwater, and the interface between the polar deposits and the underlying crust. Such observations would likely generate significant observational support to answer definitively some of the first-order questions posed above.

[4] SHARAD (SHAllow RADar) is an HF-band radar sounder that is part of the Mars Reconnaissance Orbiter (MRO) instrument payload. The spacecraft, launched successfully on 12 August 2005, will begin its primary science phase in November of 2006. Primary science objectives of SHARAD include (1) the spatial distribution and physical state of water in the subsurface of Mars, (2) the character of the Martian surface beneath the polar deposits, and (3) the structure of the polar layered deposits (PLD) [*Seu et al.*, 2004]. In this paper we concentrate on the third of these goals by developing simple dielectric models of the PLD based on their brightness variations with depth and estimates of dust or sand inclusion fractions. We apply the various PLD synthetic dielectric profiles to a wave propagation model and calculate the returned power of subsurface reflections as a function of inclusion fraction in ice. This procedure yields some basic predictions on which types of PLD features the SHARAD radar sounder might be able to detect.

[1] Lunar and Planetary Institute, Houston, Texas, USA.
[2] Department of Earth and Planetary Sciences and McDonnell Center for the Space Sciences, Washington University, St. Louis, Missouri, USA.

Copyright 2006 by the American Geophysical Union.
0148-0227/06/2005JE002609

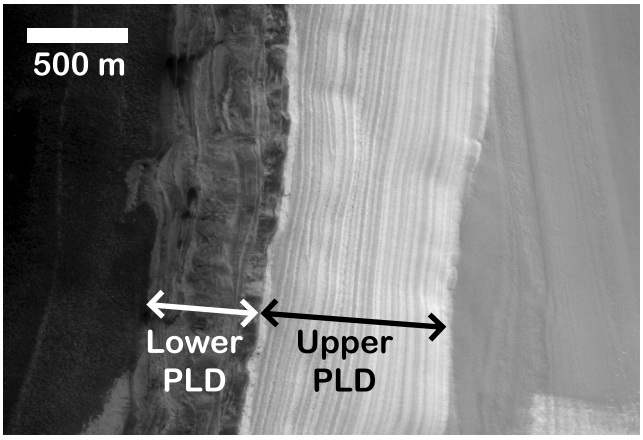

Figure 1. Section of MOC frame E0300889 showing the Upper and Lower units of the Northern PLD at local noon during northern summer (L_s = 143.29°). Coordinates of the center of the frame are 0.03°E and 85.10°N.

[5] In this paper we first review the nature and the basic properties of the polar layered deposits that are essential in constructing a model. Next we examine the dielectric behavior of the primary components of the polar caps, followed by a description of the approach used to obtain ice/silicate mixture ratios and the electromagnetic wave propagation model. Finally, we explore how different PLD compositions and thermal profiles affect the propagation of a SHARAD-like pulse and discuss the plausibility for the detection of subsurface structures.

2. Polar Layered Deposits

[6] Stratigraphy and composition are fundamental in constructing a dielectric model of the Martian polar caps. Although there are some significant differences between the northern and southern polar deposits, enough similarities exist to warrant a coarse, generic stratigraphy that is defined downward from the surface by (1) seasonal frost, (2) residual ice, (3) layered deposits, and (4) preexisting Martian surface.

[7] Seasonal polar deposits in both hemispheres consist mainly of solid CO_2 (dry-ice) and occur during local wintertime when a reduction in insolation causes the surface temperature to fall and CO_2 to condense [*Leighton and Murray*, 1966]. Seasonal ices may directly overlie residual ice, polar layered deposits, or the Martian surface per se depending on latitude [e.g., *James et al.*, 1992]. The maximum late-winter residual CO_2 ice thickness is 1–2 m at latitudes greater than 80° and monotonically thinner with decreasing latitude, and an upper limit to the average density of the CO_2 ice is 910 ± 230 kg m^{-3} [*Mitrofanov et al.*, 2003; *Smith et al.*, 2001]. The residual ice cap, in turn, differs from one hemisphere to the other. In the northern hemisphere the residual ice is H_2O, which covers and grades into most of the underlying layered deposits [*Thomas et al.*, 1992, 2000], and its albedo (∼45%) is consistent with ice bearing a small fraction of dust whose amount is hard to constrain [*Kieffer*, 1990; *Thomas et al.*, 1992]. In the southern hemisphere, however, the residual ice consists of a ∼8 meter-thick layer of CO_2 ice that covers only a fraction of the southern PLD and represents a separate geologic unit from the underlying H_2O-ice and layered deposits [*Thomas et al.*, 1992, 2000; *Titus et al.*, 2003].

[8] The polar layered deposits also differ from one pole to the other. The northern PLD (NPLD) can be divided into an upper layered unit (∼2-km thick) and a lower layered unit (∼1-km thick). The boundary between these two NPLD units is sharp and approximately constant in elevation (∼-4.3 km from datum) [*Byrne and Murray*, 2002; *Edgett et al.*, 2003], as shown in Figure 1, and it may represent an unconformity. The upper NPLD unit is relatively bright, has smooth outcrops, and consists of mostly horizontal layers that are thin (∼30 ± 15 m) and laterally uniform for hundreds of kilometers [*Byrne and Murray*, 2002; *Edgett et al.*, 2003]. Variations in albedo across these layers are frequently attributed to different volume fractions of silicate inclusions in the ice [e.g., *Thomas et al.*, 1992]. The inclusions are thought to be dust, based on their relatively high albedo and color, the lack of dunes or debris flow in polar troughs, and the observation of wind-blown streaks originating from the polar troughs [e.g., *Edgett et al.*, 2003; *Herkenhoff and Murray*, 1990; *Thomas et al.*, 1992]. In contrast, the lower NPLD unit is darker, has rough, platy outcrops, and its layers are ∼20–50 m thick and not as laterally uniform as those in the upper NPLD unit [*Byrne and Murray*, 2002; *Fishbaugh and Head*, 2005; *Malin and Edgett*, 2001]. Debris flows associated with the lower NPLD layers are the probable source of material for the polar dunes found in the Olympia Planitia [*Byrne and Murray*, 2002; *Fishbaugh and Head*, 2005], which have color, albedo, and thermal emission consistent with sand of "type II" composition, as determined by the Thermal Emission Spectrometer on the Mars Global Surveyor spacecraft [*Bandfield*, 2002; *Herkenhoff and Murray*, 1990]. The lower NPLD unit is possibly a paleo-erg, where the cementing ice may take 50% of the volume, but varying mechanical competency across layers in this unit likely reflect some variation in ice to sand ratio [*Byrne and Murray*, 2002]. Little constraint exists, however, on the silicate to ice fractions for the lower NPLD unit. Most recently, the OMEGA instrument on Mars Express has unambiguously identified a broad swath of surficial calcium sulfate deposits on the western portion of the Olympia Planitia dunes and adjacent to the perennial ice units [*Langevin et al.*, 2005a]. Gypsum best matches the spectral signature of the deposit, suggesting the past interaction of water with Ca-bearing mineral phases in the dune material. It is not clear whether the polar sulfate unit extends beneath the ice cap, but this is not implausible as the materials in the dunes likely derive from the lower NPLD unit. The mixing of sulfates in an icy matrix would likely alter the dielectric properties of the mixture.

[9] The southern PLD (SPLD) consist of a layered unit that is similar to the upper NPLD, with outcrops being smooth and layers being mostly horizontal and laterally uniform for hundreds of kilometers [e.g., *Kolb and Tanaka*, 2001]. The lack of duneforms in the southern polar troughs also suggests that albedo variations across the layering are due to varying fractions of dust (instead of sand) in ice [*Edgett et al.*, 2003]. The ice throughout the SPLD is likely H_2O, as it appears to form the lag deposits from CO_2

Table 1. Dielectric Constants of Model Constituents

Basalt Model	Reference	ε'	ε''
Generic - low value	*Ulaby et al.* [1986]	5.4	0.001
Shergottite	this study	8.8	0.017
Altered	*Heggy et al.* [2001]	15	1.500

sublimation in the residual cap [e.g., *Byrne and Ingersoll*, 2003] and has been recently detected beneath the residual CO_2 unit [*Titus et al.*, 2003]. The SPLD do not possess a lower darker, sandy unit.

[10] Finally, the PLD rest on a preexisting ancient surface in both hemispheres. In the northern hemisphere, this surface corresponds to Hesperian-aged plains deposits that overlie an Early Noachian surface [*Frey et al.*, 2002]. In the southern hemisphere, the preexisting surface is the Noachian cratered highland [*Kolb and Tanaka*, 2001]. Neutron data from Mars Odyssey show that in both hemispheres the upper ~1 m of the regolith surrounding the polar caps is rich in hydrogen and suggest a volume fraction of ice as large as 60% [*Boynton et al.*, 2002]. In this paper, however, we are mainly concerned with the PLD and only model the ground beneath the polar ice deposits as a homogeneous volume.

3. Model

3.1. Dielectric Constants

[11] In principle, there are three major components of the Martian polar caps: CO_2 ice, H_2O ice, and silicate material. The complex dielectric constant of CO_2 ice depends mainly on density and is best described by a Rayleigh mixing model [e.g., *Pettinelli et al.*, 2003]. CO_2 frost has lower density and dielectric constant than bulk CO_2 ice because of significant porosity. We calculate the complex (relative) dielectric constant for the seasonal CO_2 frost to be $\varepsilon_{frost} \equiv \varepsilon'_{frost} + i\varepsilon''_{frost} = 1.59 + i\ 9.78 \times 10^{-7}$ based on Rayleigh mixing, the bulk and estimated average frost densities (1500 kg m^{-3} and 910 kg m^{-3}, respectively [e.g., *Smith et al.*, 2001]) and the complex dielectric constant of bulk dry ice ($2.12 + i\ 2.12 \times 10^{-6}$ [e.g., *Pettinelli et al.*, 2003]). Note that we use relative dielectric constants throughout this paper, which are defined as the absolute permittivity of the materials divided by the permittivity of free space, $\varepsilon_0 = 8.85 \times 10^{-12}$ F m^{-1}.

[12] Previous studies have used constant values for the complex permittivity of pure water ice when investigating the propagation of SHARAD pulses in the Martian subsurface. *Picardi et al.* [2004], for example, adopted $\varepsilon'_{ice} = 3.15$ and $\varepsilon''_{ice} = 6.30 \times 10^{-4}$ in a generic crustal model, which is only an approximation, however, as the complex permittivity of pure water ice displays dependence to frequency and more strongly to temperature, especially in the case of ε''_{ice}. Experiments show the real component to vary between 3.14 and 3.19 and the imaginary component to vary, approximately, between 10^{-5} and 10^{-2}, depending on temperature and frequency [e.g., *Ulaby et al.*, 1986]. To assess the effects of temperature and frequency on ε_{ice} over the conditions relevant to SHARAD (center frequency, f_c = 20 MHz, and bandwidth, B = 10 MHz) and polar caps of Mars (temperature, $T > 140$ K), we investigate two dielectric models of pure water ice. *Chyba et al.* [1998] used the Debye theory of dipole relaxation and high temperature data ($T > 240$ K) to obtain a function for the permittivity that extrapolates to colder conditions. *Matzler* [1998], however, adopted results from theoretical studies that included both dipole relaxation and lattice vibrations, as well as data from a series of experiments covering a wide range of frequencies (1 MHz–1000 GHz) and temperatures (80 to 270 K). Not surprisingly, the permittivity formulas of *Chyba et al.* [1998] and *Matzler* [1998] differ substantially at temperatures below 200 K.

[13] Here we use temperature profiles for both low and high obliquity scenarios obtained from the finite difference thermal modeling results of *Larsen and Dahl-Jensen* [2000]. Their model incorporates insolation histories under different obliquities (15° and 34°), a basal heat flow of 30 mW m^{-2} (i.e., Martian average), and a constant thermal conductivity value of 1.5 W m^{-1} K^{-1}. Although the thermal state of the interior of the polar caps is not observationally constrained and the above model is based on a simplified single-unit stratigraphy, the solutions of *Larsen and Dahl-Jensen* [2000] with the different obliquities bounding the current value of ~25° lead to physically reasonable temperature profiles and should allow us to understand the importance of the effect of temperature on ε_{ice} ice and on the propagation of the SHARAD radar pulse.

[14] The real part of the dielectric constants of bulk, dry igneous materials varies by less than a factor of 10, usually ranging between 4.9 and 9.6 according to composition, and does not depend strongly on frequency [e.g., *Ulaby et al.*, 1986]. The electrical loss tangent ($\tan\delta = \varepsilon''/\varepsilon'$) of the same materials, in contrast, varies by ~3 orders of magnitude according to FeO+TiO_2 content [*Olhoeft and Strangway*, 1975]. In parts of this study we use $\varepsilon_{rock} = 8.80 + i\ 1.70 \times 10^{-2}$, which derives from applying average bulk composition and density of shergottites [e.g., *Lodders*, 1998] to the empirical dielectric relationship of *Olhoeft and Strangway* [1975] measured from lunar regolith. Recently, in situ measurements by landers and rovers show the composition of dust having a weathered component as well as Fe-bearing and sulfate phases [e.g., *Brückner et al.*, 2003; *Gellert et al.*, 2004; *Rieder et al.*, 1997; *Soderblom et al.*, 2004]. In response, laboratory studies have measured the complex permittivity of Martian soil and dust analogs of different compositions, finding density and FeO + TiO_2 content to be the strongest parameters controlling the dielectric properties [e.g., *Heggy et al.*, 2001; *Pettinelli et al.*, 2005; *Williams and Greeley*, 2004]. The samples in those analyses were either loose or compacted powders having a wide range in porosity values (>20%) and, in some cases, mixed with a small proportion of water or ice (<20%). Although such sample arrangements are more appropriate for soils and permafrost than dirty ice likely to found in the PLD units, they provide a wide dielectric range for silicate-ice mixtures. Note that the average Shergotite of *Lodders* [1998] and the altered basaltic analog of *Heggy et al.* [2001] in Table 1 correspond to FeO + TiO_2 contents of at least 18.9 and 22.2 wt%, respectively. The generic basalt from *Ulaby et al.* [1986], in contrast, does not have an associated composition, but its lower imaginary part of the dielectric constant hints at a lower iron and titanium content. Consequently, the range in oxide content associated with Table 1 is likely representative of the silicate inclusions present in

the Martian polar ices. We thus experiment with these stipulated values to appraise the interplay between ε_{incl} and layering on EM wave propagation of the SHARAD pulse.

[15] The heart of the dielectric model is the subsurface section that corresponds to the UPLD, where dust occurs in the ice in proportions that we assume can be deduced from albedo, and we use the northern PLD as the reference to our modeling. Obtaining the inclusion volumetric fraction, ν, from albedo is not straightforward nor well constrained because it depends on the size of both ice and inclusion grains [*Kieffer*, 1990]. In the following section we describe the procedure that we use to obtain plausible profiles of inclusion fraction with depth, $\nu(z)$. From the synthetic $\nu(z)$ profiles of the UPLD, mixing models such as DeLoor and Tinga-Voss-Blossey [e.g., *Ulaby et al.*, 1986] yield effective dielectric constant profiles, or $\varepsilon_{eff}(z)$, based on the dielectric constants of the mixture components, ε_{ice} and ε_{incl}.

[16] Layering is less uniform in the case of the LPLD, and the relationship between albedo and composition is not known. Therefore the technique for estimating the dielectric profile of the UPLD is not necessarily valid for the lower unit, and we assume the LPLD to be a uniform, sand-rich ($0 \leq \nu_{LPLD} \leq 1$) layer. This approach to the LPLD enables us to at least estimate signal attenuation due to conductive losses. We also use the same value of ε_{incl} in the mixing formulas to determine the dielectric constant of the LPLD as in the UPLD, with the main difference between the two units being inclusion fraction ($\nu_{LPLD} > \nu_{UPLD}$). Since the grain size of dust (2–10 μm) and sand (~100 μm) are both orders of magnitude smaller than the SHARAD wavelength (~15 m), these mixing formulas are justified for both the upper and the lower units of the PLD model.

3.2. Stratigraphic Model

[17] Creating a plausible dielectric profile for the model polar cap is the initial task in the modeling. We used imagery from both the Mars Orbiting Camera Narrow-Angle system (MOC-NA) and the Thermal Emission Imaging System's visible subsystem (THEMIS-VIS), while incorporating the topographic data from the Mars Orbiting Laser Altimeter (MOLA 115-m/pixel MEGT_N_512 grid) to construct a profile of visual albedo versus depth for a section of the Northern PLD. Our survey focused on one of the polar troughs that carve the upper unit of the NPLD and locally expose the stratigraphy of the cap. Trough stratigraphy possibly represents the structure of large portions or perhaps the overall UPLD unit [e.g., *Milkovich and Head*, 2005]. The shallow slopes of these troughs, commonly less than ~10°, intersect the subsurface layers and allow the detection of fine-scale stratigraphy that would be otherwise impossible to detect at other, steeper exposures such as arcuate scarps. Imagery and topographic data were obtained from NASA's Planetary Data System, and both radiometric calibration and map projection were accomplished via USGS's Integrated Software for Imager and Spectrometers (ISIS) software (http://isis.astrogeology.usgs.gov).

[18] We processed the THEMIS-VIS Band 3 frame V05467016 of a polar trough near the latitude of 86°N and longitudes 65°–95°E, shown in Figure 2. Of the five narrow bands composing the THEMIS-VIS system, Band 3 (650 ± 25 nm) provides the best contrast when viewing the surface. Solar longitude at the time of exposure was L_s = 149°, which corresponds to mid to late summer in the northern hemisphere and a time when bright seasonal frost deposits are no longer present in the region [e.g., *Benson and Cantor*, 2005; *James and Cantor*, 2001]. Calibrated radiances need to be divided by the cosine of the angle of sunlight incidence in the frame scene, θ = 80.1°, in order to compensate for the illumination geometry. The ratio between the incidence-corrected calibrated radiance and the solar irradiance at the given L_s yields the Lambert Albedo (A), which assumes a perfectly diffusive surface and can be seen in Figure 3.

[19] We also examined the MOC-NA frame M00-02100, which spatially coincides with our THEMIS frame (Figure 2) and encompasses a wider spectral band (700 ± 200 nm). Solar longitude at the time of frame acquisition was L_s = 124°, corresponding to near mid-summer and an absence of seasonal frost [e.g., *Benson and Cantor*, 2005; *James and Cantor*, 2001]. Calibration in ISIS of MOC radiance corrects the data for camera response, pixel variation and noise, and scales to the flux reflected by a 100% Lambertian surface at 1 AU from the Sun. This procedure yields reflectance values in percent, which are transformed into Lambert albedo by the 1/cos θ factor (θ = 69.3° in this frame) and seen in Figure 3 as well. Note that the downrange (i.e., along track) shift of ~400 m present between the MOC and THEMIS frames in Figure 2, which is due to relative uncertainties in the projection, was manually removed so as to produce consistent profiles from both data sets.

[20] A comparison of Lambert albedo profiles, $A(z)$, obtained from MOC and THEMIS illustrates the much superior spatial resolution of the Narrow-Angle MOC and a strong correlation between the two data sets, as major stratigraphic features occur at the same depth. Amplitudes of albedo variations are greater in MOC than in THEMIS in the upper part of the trough. There is certainly a pixel-averaging effect in the THEMIS albedo because of its lower resolution, but this cannot explain the lower amplitudes of some of the broader features. Two other factors may explain this difference: (1) atmospheric effects, which were not considered in obtaining the albedos, and (2) the 80° angle of incidence in the THEMIS frame is so large that the Lambertian approximation may not be entirely valid. Yet this difference is relatively minor when compared to the uniform ~0.28 difference in absolute values between MOC and THEMIS albedos. The obvious caveat is that the MOC system was designed as an imager and not as a photometer, and the reflectance values have some uncertainty [e.g., *Hale et al.*, 2005; e.g., *Malin and Edgett*, 2001]. Another point that complicates the MOC-THEMIS comparison is the different spectral range between the two systems. Using the albedo profile from THEMIS is not satisfactory because its poorer resolution would essentially impede us from assessing the effect of the fine-scale layering on the propagation of the SHARAD pulse (one of the main purposes of this paper!). This difficulty cannot be simply resolved, such that we opt to use MOC databased on the following points. The relative behavior in albedo between these two data sets at the location studied is similar and well correlated, as demonstrated in Figure 3. The range in Lambert albedo values produced from MOC in this study and encompassing

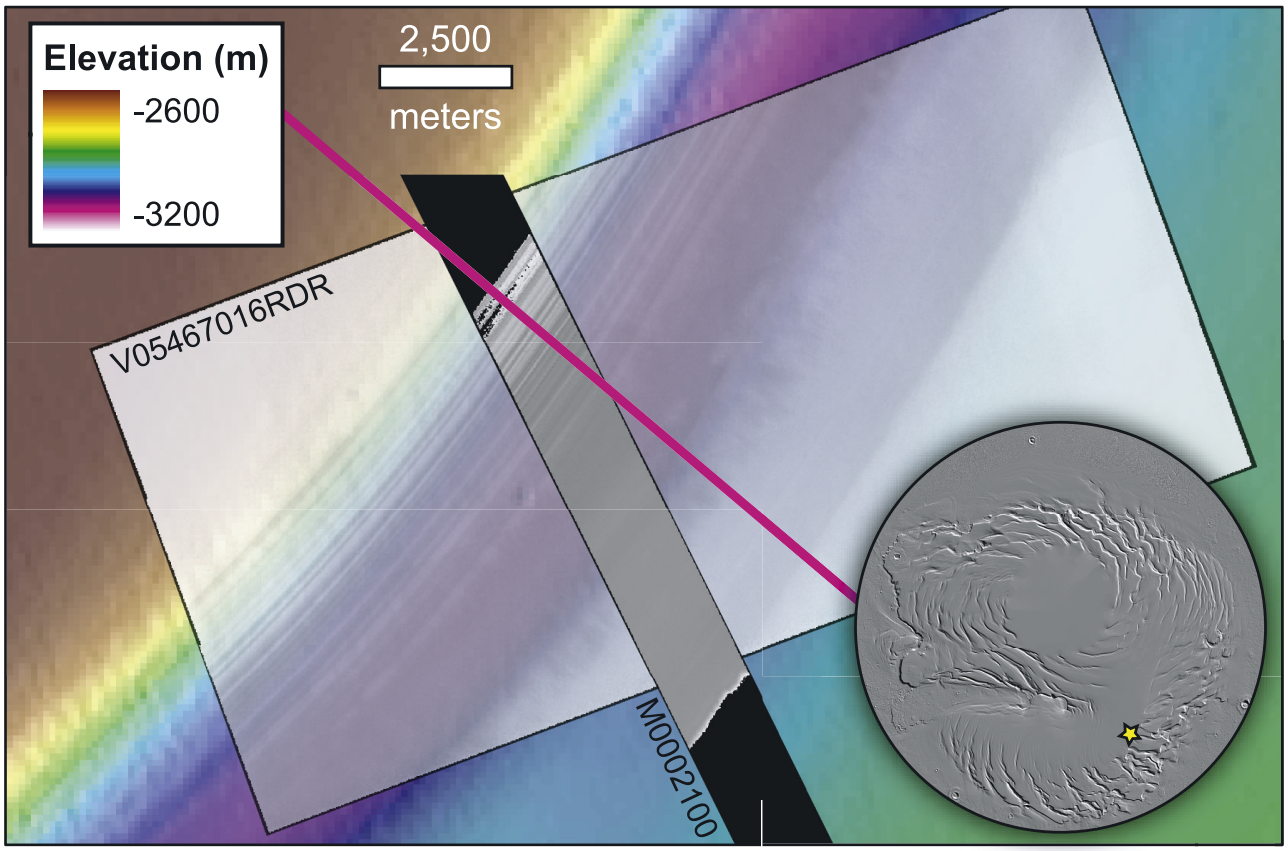

Figure 2. Background: shaded relief of northern polar trough with color encoding for elevation, based on MOLA MEGT_512_N grid; illumination is from the right. Frame is centered approximately at 80.7°E and 86.4°N. Superposed are both THEMIS-VIS and MOC-NA frames (V05467016RDR and M0002100, respectively) used in obtaining UPLD albedo. Black portions in the MOC frame are saturated pixels in the detector. The thick magenta line shows the profile adopted in Figure 3. The star in the circular inlay shows the position of the depicted polar trough on the polar cap for context.

both the PLD and the residual cap, 0.25–0.40, is comparable to the ranges in summertime albedo from other properly calibrated instruments, such as Viking's IRTM [*Bass and Paige*, 2000] and MGS's TES [*Kieffer and Titus*, 2001], albeit not as high as the residual ice estimate of 0.55. Finally, the same MOC calibration procedure to obtain albedo has been applied to MOC-WA in other studies with some degree of success [e.g., *Benson and Cantor*, 2005; *Hale et al.*, 2005].

[21] It should be mentioned that differences in pixel scale between MOLA (115 m/pixel) and MOC (3 m/pixel) and local slopes cause much pixelation in the topographic profile and an irregular sampling of albedo per unit depth. We used a 200-point averaging scheme to remove pixelation from the topographic profile and a nearest-neighbor interpolation routine to resample the albedo data at every meter in-depth. We experimented with other values for the averaging interval and sampling rates and found that the values adopted ultimately did not lead to any substantial deviation from the original data. We also extracted the upper 250 meters of the MOC profile covering most of the layering visible in the trough, and repeated it downward to produce an albedo model of the 2-km thick UPLD. Repeating the same pattern is not inconsistent with the actual cap because the layering likely follows the cyclic orbital forcing on climate and ice deposition [e.g., *Laskar et al.*, 2002].

[22] The conversion of albedo to volumetric fraction of silicate inclusions in the ice is not straightforward or unique because it strongly depends on the grain size of both ice and inclusions. The radiative transfer model of *Kieffer* [1990], summarized in part in Table 2, shows that an albedo value (e.g., $A = 0.2$) can be produced by a given inclusion fraction ($\nu = 10^{-4}$) with either "large" (ice = 1 mm, inclusion = 0.1 mm; Case I in Table 2) or "small" (0.1 mm, 10 μm; Case II in Table 2) ice and inclusion grains. The strongest controlling factor in determining ν for a given albedo is the ratio between the two grain sizes: as ice and inclusion grains become similar in size (e.g., 0.1 mm), inclusion fraction increases (0.1) to produce the same albedo (0.2).

[23] Remote sensing data as well as in situ observations constrain the size of dust to fine sand to a range approximately from 1 to 100 μm [e.g., *Herkenhoff et al.*, 2004; *Moore et al.*, 1999; *Ruff and Christensen*, 2002]. There are no direct observations of the polar ice on Mars, in contrast. Very recently, *Langevin et al.* [2005b] used infrared data from the OMEGA instrument

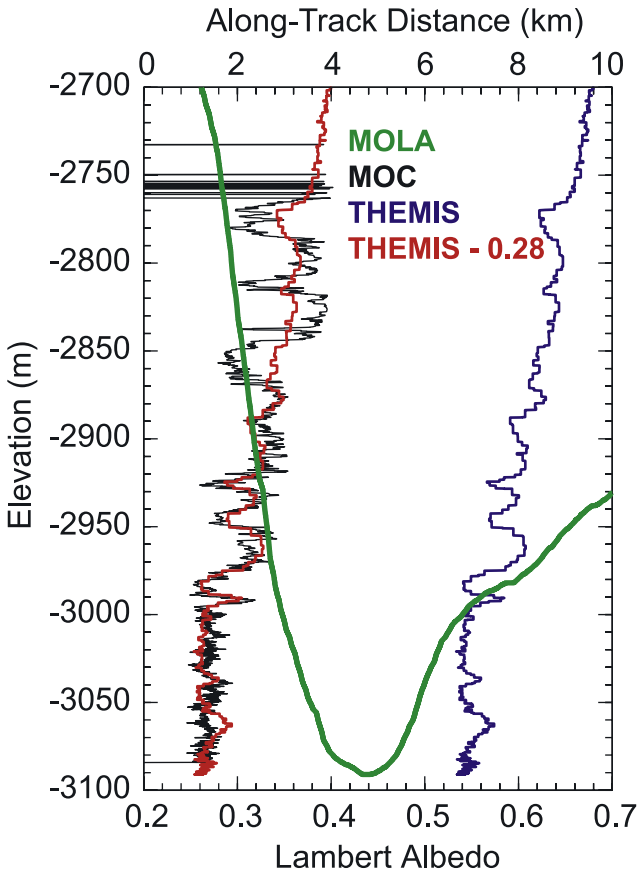

Figure 3. Lambert albedo relationship with respect to depth of the NPLD obtained from the profile in Figure 2 for both MOC (black) and THEMIS (blue). The red line is identical to the THEMIS albedo subtracted by a constant value of 0.28. The bold green line shows the topography of the trough along the profile line, and the albedo data derive from the left (northern) wall of the trough.

aboard the Mars Express spacecraft to constrain the grain size of the ice on the surface of the perennial deposits at the northern polar cap via the strength of H_2O absorption bands, and they suggested the surficial ice grain size to be on the order of 1 mm and the upper limit to dust content by volume to be 6% and possibly much lower ($\ll$1%). Due to the still poor constraints on ice/dust ratios, we adopt the wide range of compositions described in Table 2, which satisfies the radiative transfer model of *Kieffer* [1990] for the albedo interval [0.2–0.45].

Table 2. Volumetric Inclusion Fractions According to Albedo and Grain Sizes[a]

Cases	Albedo	ν	ν	ν	ν
	0.45	0.0001	0.001	0.01	0.1
	0.20	0.001	0.01	0.1	0.5
I	Ice grain	~1 mm	0.4 mm	0.2 mm	0.1 mm
	Dust grain	0.1 mm	0.1 mm	0.1 mm	0.1 mm
II	Ice grain	0.1 mm	40 μm	25 μm	12 μm
	Dust grain	10 μm	10 μm	10 μm	10 μm

[a]*Kieffer* [1990].

[24] The relationship between albedo and inclusion fraction is linear in semi-log space for the albedo range and dust grain sizes larger than 2.5 μm, as shown in Figure 7 of *Kieffer* [1990], and it allows the transformation of $A(z)$ into $\nu(z)$. Finally, the application of $\nu(z)$ into the mixing formulas described in the previous section, in conjunction with ε_{ice} and ε_{incl}, generates the UPLD dielectric model such as the one in Figure 4.

3.3. Wave Propagation and Signal Processing

[25] The wave propagation model adopted in this study is one-dimensional and follows the formulation of *Wait* [1970] for normal incidence of plane waves on layered media. The model solves the full wave equation, including the diffusive term that accounts for electric losses due to medium conductivity, as a function of frequency, f. The model domain contains M smooth and horizontal layers of thickness h_j, where the lowest layer ($j = M$) is actually a half-space. The layers in our simulations all have the same thickness $h_{j=1,M} = 2.5$ m, which is smaller than the resolvable fine-scale albedo variation in the PLD and allows for the creation of a continuous dielectric profile with depth. Permeability in our model is constant and equal to that of free space throughout, which is a good approximation for ices and silicic impurities [e.g., *Ulaby et al.*, 1986]. The tangential component of the electric field is continuous across all layer interfaces, while the normal component varies in intensity according to the contrast in dielectric

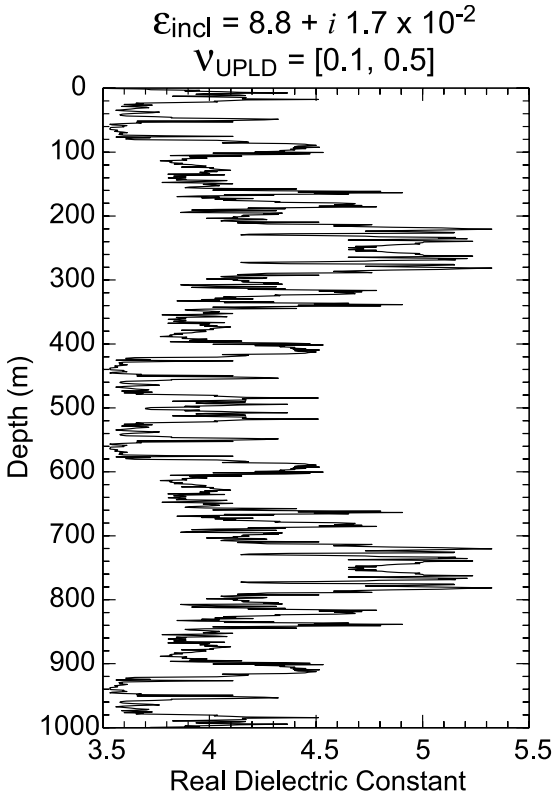

Figure 4. Example of a dielectric profile (real part shown only) obtained from the albedo and elevation data and through the application of the Tinga-Voss-Blossey mixing formula with $\varepsilon_{ice} = 3.15 + i\,6.3 \times 10^{-4}$, $\varepsilon_{incl} = 8.8 + i\,1.7 \times 10^{-2}$, and $\nu_{UPLD} = [0.1, 0.5]$.

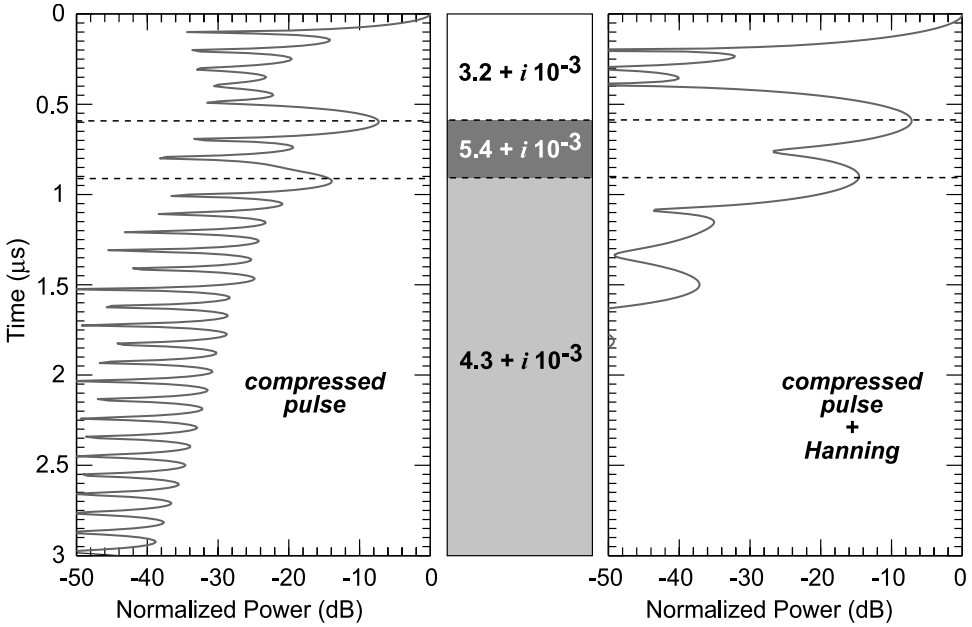

Figure 5. (center) Reflection histories or radargrams of the illustrated dielectric profile using (left) a simple compressed pulse and (right) a compressed pulse with a Hanning window. Separation between the two subsurface reflectors is 20 m, and the contrast in the real part of the dielectric constant across the lower reflector is half of that across the upper reflector. Compressed pulse parameters are those of SHARAD (f_c = 20 MHz, B = 10 MHz, τ = 85 μs).

constant across each material interface. Only downward propagating waves occur in the half-space, whereas both upward and downward propagating waves occur in the other layers. The resulting effective complex impedance, Z, captures the complete electromagnetic response of the subsurface and yields an effective Fresnel reflection coefficient $R(f)$ at the surface. This coefficient is calculated for all of the N frequencies defining the radar pulse, where $N = (B/\Delta f) + 1$, B is the pulse bandwidth, and Δf is the sampled frequency spacing. The SHARAD pulse is an up-chirp linearly modulated in frequency and defined by f_c = 20 MHz, B = 10 MHz, and pulse duration τ = 85 μs.

[26] Our simulations mimic the SHARAD range-direction data processing in that the 85 μs chirped pulse, weighted by a Hanning function in order to control reflection side lobes, is brought into the frequency domain via a Fast Fourier Transform (FFT) and multiplied by $R(f)$ to obtain the signal response of the target. The signal is "detected" with a matched filter in the frequency domain when multiplying the response of the target by the weighted chirp spectrum, at which point an Inverse Fast Fourier Transform (IFFT) of the result produces a time history of the reflected signal, generally known as a "radargram." In this paper, the times and power of subsurface reflections are referenced to the first arrival of the surface reflection (t_{surf} = 0 μs and P_{surf} = 0 dB). Note that we have not introduced Doppler information into the signal and so have not simulated the step of azimuth focusing. Thus we assume that Doppler processing would have no differential effects on the various subsurface reflections in the plane-layered model.

[27] Figure 5 illustrates two radargrams and the effect of a Hanning window applied to the signal for side lobe control. The dielectric structure in this example, outlined in the center panel of the figure, is arbitrary and consists of two subsurface reflectors separated by 20 meters, where the upper reflector consists of a dielectric contrast twice as large as the one across the lower reflector. When using a simple compressed pulse (left), both reflectors are resolved: the upper reflector (0.6 μs) stands 14 dB higher than neighboring side lobes, while the lower (0.9 μs) is only 6 dB stronger than adjacent side lobes. Applying a Hanning window to the signal causes the reflection peaks to stand at least 20 dB higher than neighboring side lobes, but both peaks are now twice as broad (~0.4 ms) than in the previous case, and they clearly begin to interact. We repeated the same exercise for smaller separations between the two subsurface reflectors and found that both are barely resolvable when placed 10 meters apart and coalesce into one even broader peak if their separation is reduced further. The minimum separation for distinct identification depends on the relative strength of the two peaks (a weak peak will tend to merge with a strong peak at larger separations than two strong peaks). As mentioned, we apply a Hanning function here to mimic the nominal processing steps to be taken with SHARAD data. The Hanning function is most useful in detecting very weak subsurface signals in the presence of the sidelobes of the strong surface reflection. This may not be an optimal weighting function for data from polar regions, where subsurface signals may be only modestly weaker than the surface signal [*Picardi et al.*, 2005], and the resolution of internal layering will be an important goal.

[28] The SHARAD system had a design requirement of 50 dB of dynamic range of the useful signal [*Seu et al.*, 2004], and in fact the actual radar in orbit around Mars (but not yet operating) performs at this level (E. Zampolini, personal communication, 2005). The dynamic range is

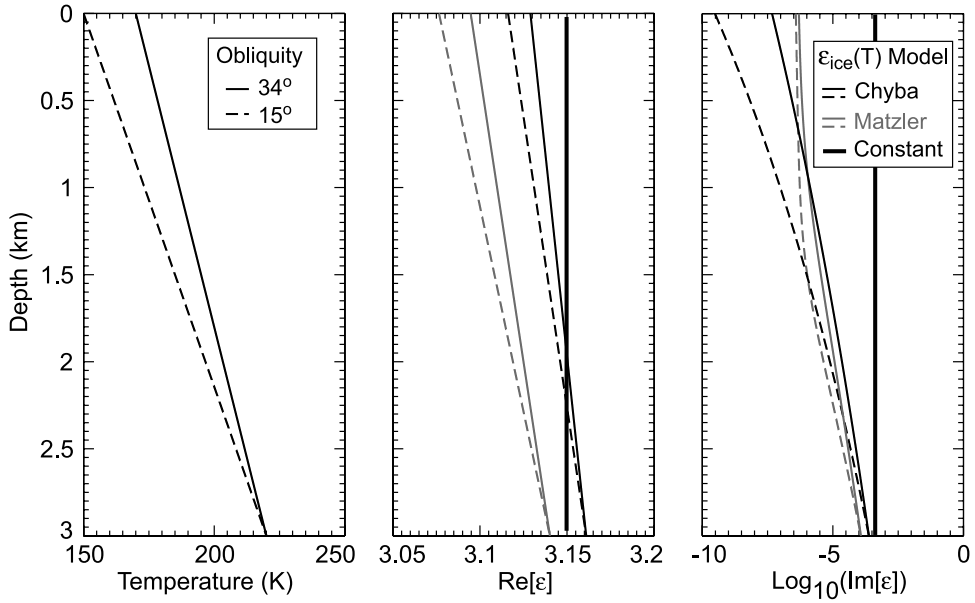

Figure 6. The effect of (left) the two end-member thermal models of *Larsen and Dahl-Jensen* [2000] on the (center) real and (right) imaginary parts of the dielectric constant of pure water ice following the models of *Chyba et al.* [1998] and *Matzler* [1998]. Thick vertical lines in the dielectric graphs represent the constant value of ε_{ice} adopted by *Picardi et al.* [2004].

based on the power in a range and azimuth focused signal being 50 dB above the galactic noise floor. The link (signal-to-noise ratio) equation calculation is based on known hardware parameters and a specular surface reflection with a dielectric constant of 3. As our model subsurface signals are normalized to the strength of the model surface reflection, we must adjust the subsurface reflection detection limit when the model surface dielectric constant differs from 3.

4. Results

[29] In this section we initially contrast the effects of temperature dependence versus a constant average of the dielectric constant of water ice, followed by the analysis on the contribution of different silicate loads and dielectric constants on the propagation of the SHARAD pulse through the model PLD. The last portion of this section deals with the variation in the PLD subsurface reflection induced by a thin surface veneer of CO_2 frost.

4.1. Temperature-Dependent Dielectric Constant of Water Ice

[30] The thermal models of *Larsen and Dahl-Jensen* [2000] consider a 3-km thick ice sheet with a constant thermal conductivity of 1.5 W m^{-1} K^{-1} and a basal heat flow of 30 mW m^{-2}, for which two solutions are presented in Figure 6. These two solutions, differing by input obliquity values of 15° and 34°, offer an upper and lower bound to the temperature distribution in the cap and go into producing dielectric constants from the *Chyba et al.* [1998] and *Matzler* [1998] ice dielectric models. Higher temperatures, resulting from greater depths or warmer surface conditions, correspond to enhanced ε_{ice} values in either dielectric model. Variations in ε'_{ice} due to temperature are relatively minor (~3%), with the Chyba model producing lesser values than the Matzler model at all depths. When adopting these same dielectric and thermal models, however, the imaginary part ε''_{ice} varies by 2.5 to 6 orders of magnitude between the surface and a depth of 3 km. Much of the temperature-induced ε''_{ice} difference between the Chyba and Matzler formulations occurs near the surface where the temperature is low, with values converging to within one order of magnitude below a depth of 1 km for all conditions tested. Included in Figure 6 for comparison is the constant value $\varepsilon_{ice} = 3.15 + i\ 6.30 \times 10^{-4}$ used by *Picardi et al.* [2004] (solid, vertical lines). Variations in ε''_{ice} between solutions for 15 MHz and 25 MHz, the lowest and highest frequency in the SHARAD frequency band, respectively, differ by less than a factor of two in both the temperature-dependent dielectric models. This effect is relatively small, and the solution for $f_c = 20$ MHz is deemed adequate for simulations of SHARAD pulse propagation in the Martian polar caps.

[31] Figure 7 incorporates the different thermal and dielectric models from Figure 6 and portrays them in the context of arrival time and normalized power. The reflections correspond to the UPLD-LPLD unconformity at a depth of 2 km; the UPLD in these examples are composed of clean (pure) ice, and the LPLD an ice-silicate mixture with $\nu = 0.5$. The contrast among the Chyba and Matzler models and the constant value of *Picardi et al.* [2004] is very minor overall: about 0.25 μs in arrival time and 3 dB in reflection power. Hence the variations in ε_{ice} induced by temperature can be neglected and the constant value adopted by *Picardi et al.* [2004] is a good approximation in view of polar cap temperatures and SHARAD frequencies. In the following section we demonstrate further that the delay in reflection arrivals and changes in transmission losses due to the small variations in ε'_{ice} are both minimal, while changes in ε''_{ice} are more noticeable in attenuating radar waves

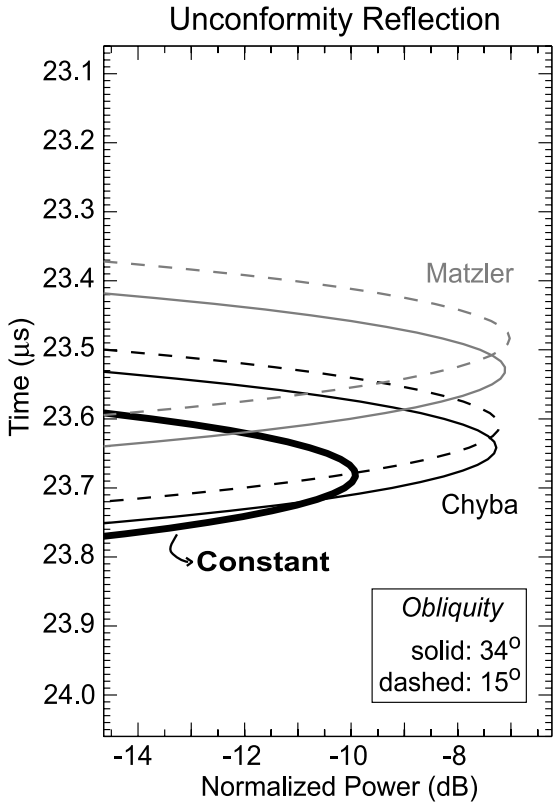

Figure 7. Unconformity reflections for the different obliquity values (solid and dashed) and ice dielectric models (different shades) used in Figure 6. The UPLD in these simulations consist of pure ice, while the LPLD are a mixture of ice and silicates with $\nu = 0.5$. The constant model stands for $\varepsilon_{ice} = 3.15 + i\ 6.3 \times 10^{-4}$ at all depths.

traveling through the layered ice column. Yet, the wider range in dielectric properties of silicate inclusions (Table 1) imposes far greater influence on radar propagation than selecting either model or the constant value for ε_{ice}.

4.2. PLD Detection and the Dielectric Constant of Silicate Inclusions

[32] Our principal goal resides in determining the plausibility of detecting fine-scale layering as well as the major units in the PLD as a function of inclusion fraction throughout the ice column. The reflection history graphs, or radargrams, in Figure 8 illustrate the detection of the UPLD as a function of high inclusion fractions and the complex dielectric constant of the inclusions. The shaded portions in each of these graphs show normalized power levels that are potentially not detectable, as they lie beneath the expected SNR-imposed performance of the SHARAD system or 50 dB weaker than a specular surface reflection with a dielectric constant of 3. We calculate the average ε'_{eff} down to a depth comparable to the free-space radar center-wavelength (15 m) and adjust the detection level accordingly if this value differs from 3. For example, if $\varepsilon'_{eff} > 3$, then the detection level (or the dynamic range of the usable signal) shifts to a lower relative power as the strength of the surface signal increases and the subsurface signal does not relative to the galactic noise floor. In actuality, the detectability thresholds in our calculations are close to −50 dB, and little variation exists because the near surface ice is bright and relatively devoid of inclusions (hence $\varepsilon'_{eff} \rightarrow \varepsilon'_{ice} = 3.15$). Not considered here are relative differences of nonspecularity between the behavior of the surface and subsurface reflectors. Note also in comparing Figures 5 and 8 that, on average, individual layers thinner than ∼20 m cannot be discerned individually and merge with other stronger adjacent reflections. Determining which individual reflectors merge into a single peak depends on relative peak strengths as set by the dielectric profile adopted for a given simulation.

[33] Large ν values lead to more prominent layer UPLD reflections because of higher contrasts in resulting dielectric constant across layers of different dust contents. In the case of low-dielectric inclusions ($5.4 + i\ 10^{-3}$), shown in Figures 8a and 8b, the strongest UPLD reflections increase from −30 dB to −20 dB by increasing $\nu_{\min}$ from 10^{-2} to 10^{-1}. For these same two cases, the layering in the UPLD is detected all the way down to the UPLD-LPLD unconformity with little loss in power, which is dominated by transmission losses across interfaces. Cases with a high dielectric constant for the inclusions ($15 + i$ 1.5), shown in Figures 8c and 8d, lead to efficient signal attenuation as a result of conductive losses, and only the upper portion of the UPLD can be detected: about 1.2 km (15 μs) when $\nu = [10^{-2}, 10^{-1}]$, and only ∼250 m (4 μs) when $\nu = [0.1, 0.5]$. In cases of the intermediate value for inclusion dielectric constant in Table 1, $8.8 + i\ 1.7 \times 10^{-2}$ and not illustrated in Figure 8, the detection of the whole of the UPLD is permissible even in the dustiest of cases. In addition, we have found that the ice in the UPLD should have a minimum fraction of dust greater than 10^{-3} if the layering is to be detected, considering the range in inclusion dielectric constants in Table 1. For example, if $\nu = [10^{-3}, 10^{-2}]$ and $\varepsilon_{incl} = 5.4 + i\ 10^{-3}$, then the strongest reflections in the UPLD have amplitudes of −47 dB, which are not likely to be detected because they barely exceed the adjusted detection level of −49.9 dB. Increasing ε_{incl} to $8.8 + i\ 1.7 \times 10^{-2}$ and to $15 + i$ 1.5 while holding $\nu = [10^{-3}, 10^{-2}]$ leads to maximum UPLD reflections of −43.5 dB and −40.5 dB, respectively, and enhances detectability.

[34] The repetitive stratigraphy of the UPLD model, generated by stacking a 250-m section of the albedo profile in Figure 3, is observed in the radargrams in Figure 8, except for 8d where attenuation permits the detection of the upper 250 m only. Distortion or obliteration of the repetitive pattern with depth is not substantial and suggests that multiple reflections of shallower UPLD layers do not interfere greatly with the primary reflections of deeper UPLD layers. To confirm this suggestion, we created three stratigraphic test cases differing only by the depth at which we forced the UPLD to have a fixed dielectric constant (i.e., no layering) down to the depth of the unconformity: 250 m, 500 m, and 2 km. In all of these three scenarios, only cases that have the highest dust loading, $\nu = [0.1, 0.5]$, produce multiple reflections above the adjusted detection level of SHARAD and their strength increases by ∼10 dB from the 250 m to the 2 km stratigraphic truncation: multiple reflections arriving immediately after the last primary reflection above the truncation have an average power of −45 dB and −35 dB, respectively. These values

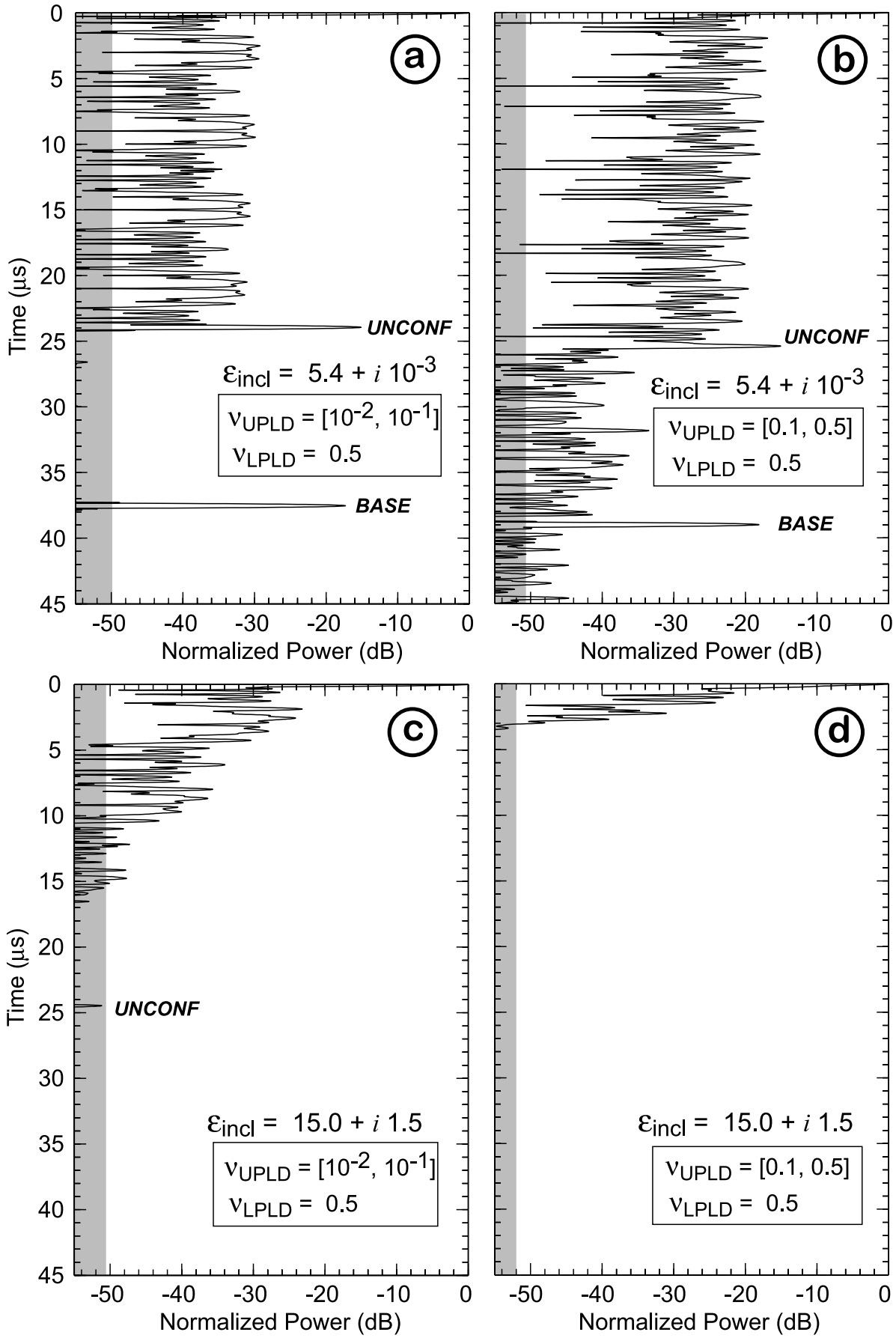
a
b
c
d
UNCONF
BASE
ε_{incl} = 5.4 + i 10^{-3}
ν_{UPLD} = [10^{-2}, 10^{-1}]
ν_{LPLD} = 0.5
ν_{UPLD} = [0.1, 0.5]
ε_{incl} = 15.0 + i 1.5
Time (μs)
Normalized Power (dB)
0
5
10
15
20
25
30
35
40
45
-50
-40
-30
-20
-10
0

Figure 8

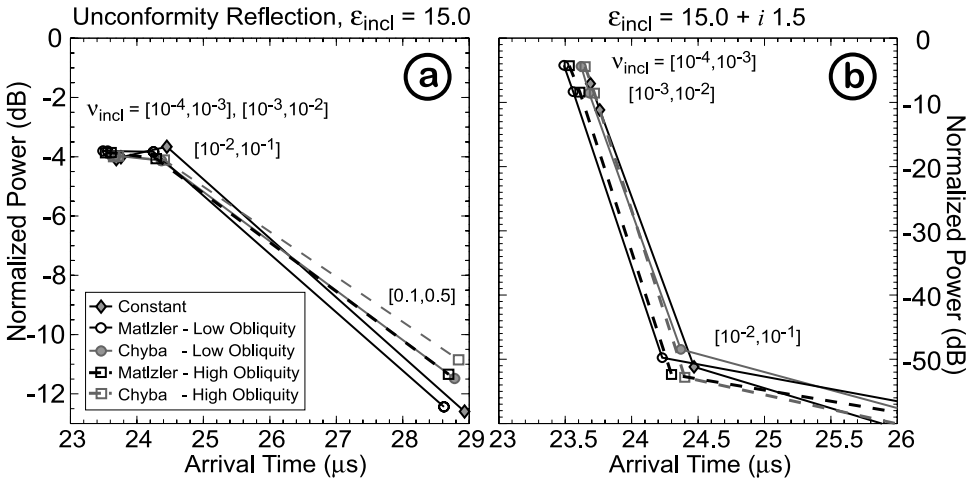

Figure 9. (a) Strength and arrival time of the reflection produced by the UPLD-LPLD unconformity as a function of inclusion fraction and dielectric model of pure ice and using real dielectric constants only ($\varepsilon'' = 0$). All cases illustrated use $\varepsilon_{incl} = 15$. (b) Same cases as in Figure 9a but now using complex dielectric constants; $\varepsilon_{incl} = 15 + i\ 1.5$. Data points below −55 dB represent the detection of noise or side lobes instead of the signal produced by the unconformity, as the unconformity does not produce an observable reflection.

correspond roughly to 25 dB and to 15 dB below the power of the primary reflections, respectively, and confirm that multiple reflections are not problematic in the UPLD for the conditions examined in this paper. Multiple reflections are not observed in the case of highly dielectric inclusions because of severe conductive losses.

[35] The conditions that lead to the detection of the two major subsurface interfaces, namely the unconformity between the upper and lower units of the PLD and the base of the polar cap, are somewhat more speculative because of the mostly unconstrained composition of the lower unit. Here we have assumed it to consist of a mix of equal volumes of ice and sand ($\nu = 50\%$). With that in mind, the unconformity is detected in all of the low and intermediate ε_{incl} cases at approximately 24 μs, with the reflection being stronger when the ice in the UPLD is the cleanest because conductive and transmission losses are minimized and the dielectric contrast across the interface maximized. Increasing the UPLD dust content from [10^{-2}, 10^{-1}] to [0.1, 0.5] reduces the unconformity reflection from −15 dB to −18 dB. Note that under minor loading of the ice with dielectrically strong inclusions (Figure 8c), the reflection produced by the unconformity is at the detection limit (−51 dB) while reflections from lower portions of the UPLD are totally suppressed. No features are detected below a depth of ∼250 m (∼3 μs) in the dustiest of the dielectrically strong cases because the signal is completely attenuated. The reflection produced by the base of the model cap, where a transition from 50% to 100% silicate content by volume is applied, is not present in under any of the strongly dielectric cases tested because of strong conductive losses in the uniform LPLD.

[36] To better understand the contribution from the different loss mechanisms, we summarize in Figure 9 the power and arrival time of the unconformity reflection from all of the simulations performed on the model PLD with the strongest value of silicate dielectric constant in Table 1 ($\varepsilon_{incl} = 15 + i\ 1.5$). To separate the effects of path loss from interface loss, we contrast cases with $\varepsilon''_{incl} = 0$ (Figure 9a) and $\varepsilon''_{incl} = 1.5$ (Figure 9b). In Figure 9a, signal attenuation is due only to transmission loss across interfaces. In nearly dust-free ice (ν = [10^{-4}, 10^{-3}]), unconformity reflection arrival and power are ∼23.5 μs and −4 dB, respectively. Increasing dust content by 2 orders of magnitude (ν = [10^{-2}, 10^{-1}]) causes both a very modest delay and a loss in power with respect to the clean ice case, and shows the minor effect of ε'_{ice} on the propagation at fractions smaller than 0.1. It is only when UPLD ice is laden with sediment (ν = [0.1, 0.5]) that a delay in arrival time and a reduction in reflection power become more substantial. The delay to ∼29 μs (about 20% increase) results from the higher value of ε'_{eff} from the entire UPLD. The weaker reflection of all of these sediment-rich models, averaging −11 dB, stem from greater transmission losses across the layering and a weaker contrast in dielectric constant across the unconformity. Note that different ice models have only minor influence over signal propagation when compared to ε_{incl} and ν, and that the constant value of ε_{ice} from *Picardi et*

Figure 8. Radargrams of the model PLD using $\varepsilon_{ice} = 3.15 + i\ 6.3 \times 10^{-4}$ and $\nu_{LPLD} = 0.5$. Crustal dielectric value is the same as that of inclusions, but corrected for an ice-free solid body. Shaded regions represent the zone below the radar detection level. When present, reflections from the UPLD-LPLD unconformity and the base of the PLD are labeled "*UNCONF*" and "*BASE*," respectively. (a) Low UPLD content of dielectrically weak inclusions. (b) High UPLD content of dielectrically weak inclusions. (c) Low UPLD content of dielectrically strong inclusions. (d) High UPLD content of dielectrically strong inclusions.

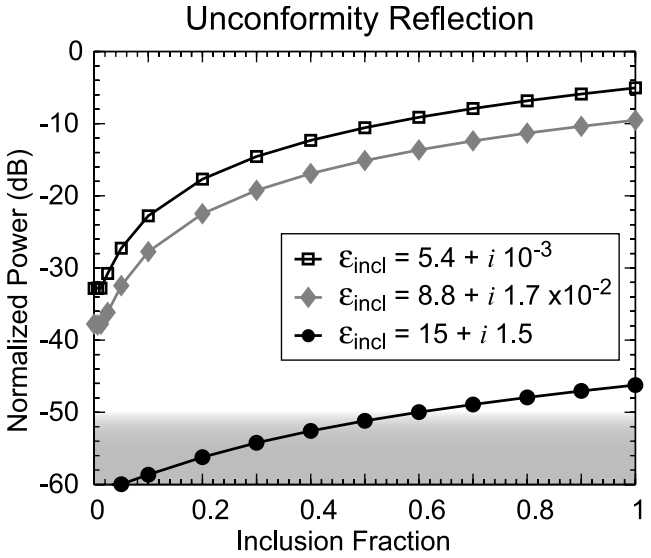

Figure 10. Strength of the reflection produced by the UPLD-LPLD unconformity as a function of dielectric constant of inclusions and their volumetric fraction in the LPLD. All cases illustrated adopt $\nu_{UPLD} = [10^{-2}, 10^{-1}]$ and $\varepsilon_{ice} = 3.15 + i\,6.3 \times 10^{-4}$. The shaded lower portion of the graph represents approximately the levels of reflected power below the detection level of SHARAD.

al. [2004], as suggested in the previous section and in Figure 7, is indeed a good approximation in the context of SHARAD and the Martian polar caps.

[37] Incorporating the imaginary part of dielectric constants in the model imposes dramatic changes, as seen in Figure 9b. Reflection power is essentially unchanged from the purely real case for the lowest UPLD dust fraction content. This observation, aside from showing that the integrated effect of weakly conducting ice is negligible, points out that dust fractions in ice of less than 10^{-2} have very little effect on the propagation even when the inclusions are strongly conductive (high ε''_{incl}). Inclusion fractions ranging from 10^{-2} to 10^{-1} in conjunction with highly dielectric inclusions depress the unconformity reflection power to about −50 dB, and a further increase of dust in the UPLD produces too much attenuation for the unconformity to be detected (peak determination routine cannot pick the nonexistent interface reflection peak and randomly selects noise or sidelobes at much later arrival times and power below −55 dB). Hence the contrast in reflection power between purely real and complex dielectric cases demonstrate that conductive losses dominate signal attenuation, except in cases where ε_{incl} takes the lowest value in Table 1.

5. Discussion

[38] A major simplification in this study, so far, has been a constant volumetric proportion of inclusions in the ice throughout the LPLD, set to 0.5 following *Byrne and Murray* [2002]. Their estimate was greatly speculative, however, and there is a dearth of observational support for this value of inclusion fraction in the lower unit. The major difficulty in modeling the LPLD descends from the radiative transfer method of *Kieffer* [1990] because, even if given host and inclusion grain sizes, it cannot determine a specific value for the inclusion fraction if the albedo of the mixture approaches that of the inclusion material itself, as in the case of the lower unit of the northern PLD. Furthermore, the fine layering observed in this much darker unit is detected mostly because of differential erosion, scarping, and much less so in terms of albedo [e.g., *Byrne and Murray*, 2002; *Edgett et al.*, 2003; *Fishbaugh and Head*, 2005]. Hence we conclude that our approach for converting albedo to inclusion fraction used in the case of the UPLD is not valid here, and it is prudent to investigate the dependence of the unconformity reflection as a function of the silicate inclusion fraction in the LPLD.

[39] The three curves in Figure 10 show the variation in power of the unconformity reflection as a function of ν_{LPLD} and for the adopted range in inclusion dielectric constants given in Table 1, while maintaining $\nu_{UPLD} = [10^{-2}, 10^{-1}]$. Examples of unconformity reflection peaks are clearly visible in Figures 8a and 8b, where they are labeled "*unconf*". Overall, reflection power increases with ν_{LPLD} because of a greater dielectric contrast between the upper and lower units. The reflection peak is resolvable for ν_{LPLD} values as low as 0.04; smaller values do not lead to enough of a dielectric contrast across the unconformity to produce a reflection, as the peak associated with the unconformity is relatively so weak that it either merges with the lowest UPLD peak or it becomes indistinguishable from secondary reflections from the UPLD. Note that for $\varepsilon_{incl} = 15 + i\,1.5$ the reflection strength is below the detectability threshold of approximately −50 dB for $\nu_{LPLD} < 0.6$ even though a reflection peak is resolvable (see Figure 8c for the radargram). Increasing the UPLD dust content to [0.1, 0.5] weakens the unconformity reflection relative to the UPLD reflections that are shown in Figure 10 and prevents a positive peak identification for the unconformity for $\nu_{LPLD} < 0.4$ with the lowest two values of ε_{incl}. This is a result of the unconformity peak not being distinguishable from UPLD primary or secondary reflections. No unconformity reflections are visible when this dustiest UPLD case is tested with the highest inclusion dielectric constant due to severe signal attenuation in the upper few hundred meters of the cap.

[40] In the event that the fine layering in the LPLD represents substantial variations in dielectric in addition to mechanical properties, our simulations set specific limits for this lower-unit layering to be detected. Obviously, enough signal power must reach the depth of the LPLD, which does not occur in cases where strong signal attenuation takes place in the UPLD due to high loading of dielectrically strong dust in the upper-unit ice (Figure 8d). Additionally, reflections in the LPLD must be stronger than the secondary (multiple) reflections produced by the UPLD layering, some of which would arrive concurrently with primary LPLD reflections. Secondary UPLD reflections increase in power with grater values of either ε'_{incl} or ν_{UPLD}. In the case of Figure 8b, $\varepsilon_{incl} = 5.4 + i\,10^{-3}$, $\nu_{LPLD} = 0.5$, and $\nu_{UPLD} = [0.1, 0.5]$, secondary UPLD reflections arriving after the unconformity signal have powers of up to approximately −37 dB. If $\varepsilon_{incl} = 8.8 + i\,1.7 \times 10^{-2}$ and $\nu_{UPLD} = [0.1, 0.5]$ characterize the UPLD, then these secondary reflections reach −32 dB and only 10 dB separates primary and

secondary reflections near the unconformity. Hence the detection of possible structure in the LPLD is only likely if the effective dielectric constant of the upper unit is relatively low, either due to low volume fractions (< 0.5) or dielectric constant of inclusions (<15 + i 1.5).

[41] Extrapolating this discussion to the likelihood of detecting and identifying the base of the polar deposits is extremely difficult because this interface is not characterized where the LPLD are present. In and near Chasma Boreale, for instance, it is not clear where the LPLD end and the Hesperian Vastitas Borealis deposits begin [e.g., *Fishbaugh and Head*, 2005]. To complicate matters, data from the Gamma Ray Spectrometer aboard the Mars Odyssey spacecraft suggest that the near surface of the circumpolar regions may contain water ice by as much as 60% in volume [*Boynton et al.*, 2002], in which case there might not be a substantial or sharp contrast in dielectric properties between the LPLD and underlying Hesperian deposits. All we can say is that enough radar energy should reach this interface in the case where the UPLD and the LPLD contain inclusions of low or moderate dielectric constant (Table 1). Two exceptions are possibly (1) at places where the UPLD overlie directly the Hesperian surface in the north and (2) throughout the southern cap as it lacks a sediment-rich lower unit and appears to contact the Noachian surface directly. In these two cases, our discussion of the north PLD unconformity should also apply, and ice-crust interfaces are likely to be observed as long as the inclusions in the ice are weaker than our $\varepsilon_{incl} = 15 + i\ 1.5$ example.

[42] Seasonality may also play a role on the propagation of radar waves through the Martian polar caps. From fall through spring a layer of CO_2 frost is deposited and later removed from the surface of both polar caps. As mentioned in section 3.1, we estimate the dielectric constant of this frost layer to be $\varepsilon_{frost} = 1.59 + i\ 9.78 \times 10^{-7}$, which is substantially lower than that of pure or dusty ice and should cause a reduction in absolute power reflected from the surface and a relative strengthening of subsurface reflections. The thickness of this layer, <10 m, is slightly smaller than the wavelength (12 m) of the center frequency of the SHARAD signal in this CO_2 medium, and it leads to a somewhat complicated behavior of the propagation phenomenon. The power of a subsurface reflection beneath a thin layer oscillates as a function of layer thickness (h_L), real dielectric constant (ε'_L) and magnetic permeability (μ_L) of the layer, and radar center frequency (f): 1 cycle $\Longleftrightarrow$ $2f h_L \sqrt{\mu_L \varepsilon_0 \varepsilon'_L}$ [*Ward et al.*, 1968]. Applying the appropriate permittivity and permeability values and the SHARAD center frequency to this formula leads to a complete oscillation in power over 5.9 m in layer thickness.

[43] To investigate further the effect of a surface CO_2 frost on subsurface reflections, we added such a layer to the surface of the full PLD stratigraphic model and varied its thickness. Figure 11 shows the reflected power from the UPLD-LPLD unconformity produced with the SHARAD pulse for three different UPLD sediment inclusion cases. In all of them, the oscillatory behavior is nearly identical, with the strongest peak occurring at $h_L = 9$ m, which closely matches the periodicity value obtained from *Ward et al.* [1968] (i.e., 5.9 × 1.5), and causing an average power increase of 22 dB over the case lacking the CO_2 layer. In contrast, a thick layer ($h_L \geq 30$ m) augments reflection power by an average of 8 dB only. The behavior described for the unconformity reflection occurs for other subsurface reflectors as well, although we only verified enhanced PLD magnitudes by visually comparing radargrams. This result also offers an interesting possibility of amplifying weak subsurface reflections as winter progresses and the frost layer thickens. Take, for example, the case of $\varepsilon_{incl} = 15 + i$ 1.5 and $\nu_{UPLD} = [10^{-2}, 10^{-1}]$ (Figures 8c and 10). In the absence the frost layer, the unconformity reflection lies just below of the adjusted detection level of SHARAD. If a layer of CO_2 is emplaced at the surface with a thickness close to 2.9 m, 6 m, or 15 m, then the increase in power causes the reflection to stand above the adjusted dynamic range by at least ~10 dB and likely making the unconformity detectable. Note that the dynamic range of the useful signal increases in power with layer thickness because the effective surface dielectric constant within the top 20 m decreases, and it causes the unconformity reflection to again lie beneath the detection limit for $h_L \geq 27$ m.

[44] Variations in CO_2 frost thicknesses may vary geographically as well as temporally. Figure 11 shows that a difference of a couple of meters in frost thickness may lead to great differences in subsurface reflection power. It is not implausible to believe that, at any given time, frost thickness may vary by that much from one location to another as a result of different deposition rates or surface topography. Spots on the cap possessing the appropriate frost thickness for power amplification may appear only at a couple of times during the Martian year. It will be necessary to cover the same area with multiple spacecraft passes throughout a seasonal cycle to identify a reflector as a weak one made visible by this natural amplification system.

[45] It is plausible that ices other than H_2O may be present at depth throughout the volume of the PLD. *Mellon* [1996] demonstrated that CO_2 and CO_2 clathrate-hydrate ices are possible for a wide range in conditions in the Martian polar caps, where a 4-km polar deposit could have as much as 36% and 72% by volume of either of these respective ices as random inclusions in water ice. Applying the dielectric constant of bulk CO_2 ice ($2.2 + i\ 2.12 \times 10^{-6}$) to a volumetric fraction of 36% in water ice yields an effective dielectric constant of $2.75 + i\ 3.75 \times 10^{-4}$, according to the Tinga-Voss-Blossey mixing formula of randomly distributed spherical inclusions. If the UPLD were to contain this much CO_2 ice in its volume, then the unconformity reflection would arrive ~1.6 μs earlier than in the pure water ice case. The unconformity reflection would be stronger due to a greater contrast in dielectric constant between the UPLD and the LPLD and a negligible conductivity. In the case of $\nu_{LPLD} = 0.5$ and $\varepsilon_{incl} = 8.8 + i\ 1.7 \times 10^{-2}$, the enhancement in power is about 3 dB. The dielectric constant of CO_2 clathrate-hydrate is not as well characterized in the literature, however, perhaps due to experimental difficulties generated by its volatility. Nonetheless, this is a lattice type I clathrate with a nonpolar guest molecule, and the real part of its dielectric constant is not likely to differ substantially from that of H_2O ice [*Davidson*, 1973]. Taking experimental values for the structurally similar N_2 clathrate from *Davidson* [1973] as a proxy, the complex dielectric constant for 20 MHz and 230 K is approximately $2.85 + i\ 4.67 \times 10^{-3}$. Using the upper limit of 72% for volumetric fraction of clathrates in the polar

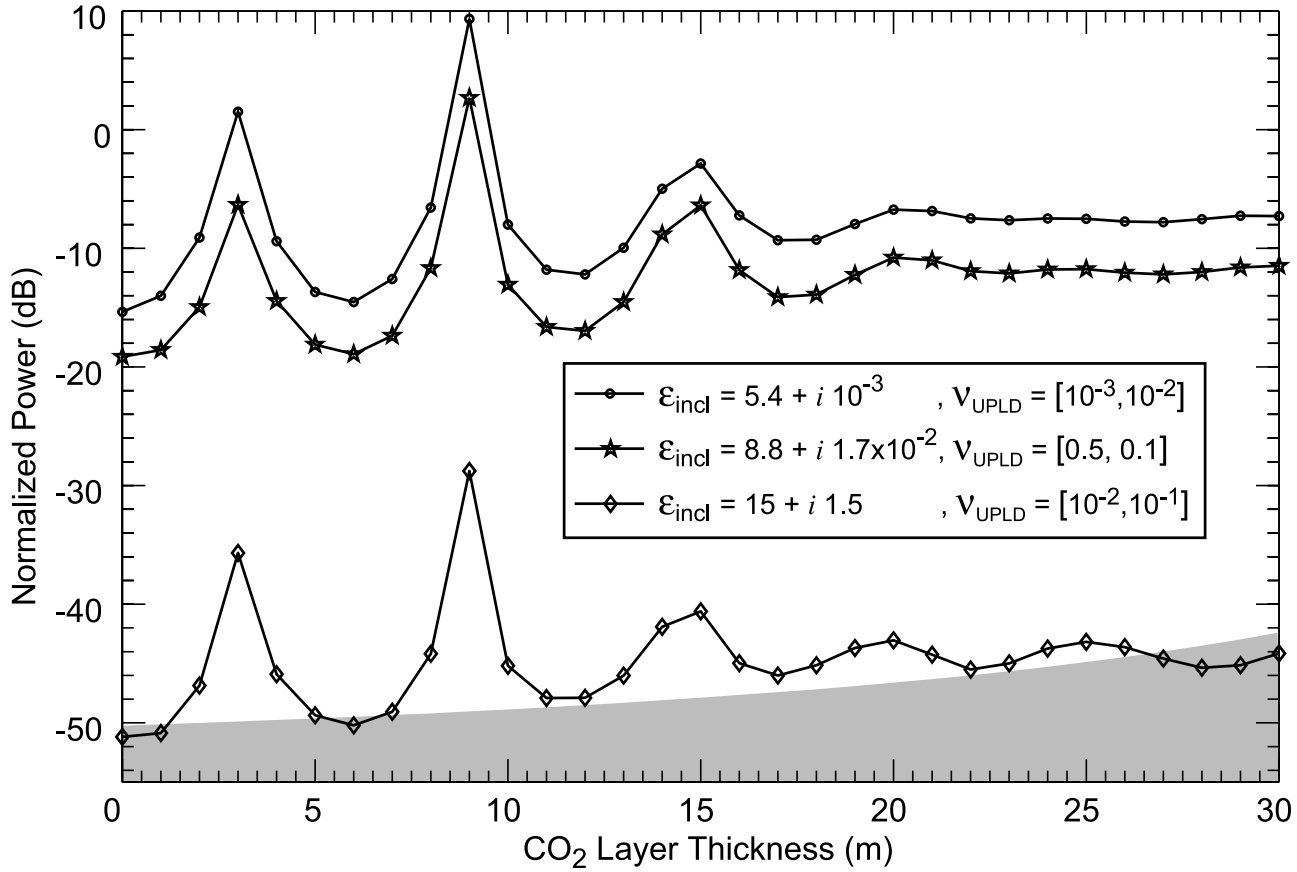

Figure 11. Normalized power of the unconformity reflection as a function of the thickness of a CO_2 ice layer overlaying the UPLD for three different combinations of silicate inclusion fraction and dielectric constant. In all three cases illustrated, $\nu_{LPLD} = 0.5$ and $\varepsilon_{ice} = 3.15 + i\ 6.3 \times 10^{-4}$. The shaded lower portion of the graph represents approximately the levels of reflected power below the detection level of SHARAD.

deposits, the effective dielectric constant becomes $2.93 + i\ 3.61 \times 10^{-3}$, which leads to an advancement in reflection of 0.8 μs. The reflected power from the unconformity is reduced by 11 dB due to the higher conductivity of the composite ice-clathrate. Hence it is clear that mixtures of water ice with dry ice and CO_2 clathrate-hydrate play a more noticeable effect on the response to the SHARAD signal than temperature-induced variations of pure water ice. These effects will be minimized, however, if secondary ices occur in distinct layers and amount to a smaller overall volume of the polar deposits. If that is the case, reflectors will likely be observed at depth, but they will not necessarily be associated with the albedo layering observed at the troughs.

[46] Finally, we demonstrated in section 4 that variations in the dielectric constant of pure water ice caused by a quasi-linear temperature gradient from 140 K to 220 K are not substantial enough to affect radar propagation. The finite difference thermal model of *Larsen and Dahl-Jensen* [2000] is simplistic when compared with the actual cap itself, for it assumes a constant value of the thermal conductivity throughout the model. It is likely that average thermal conductivities differ between the ice-rich upper unit and the sandy lower unit, being higher for the latter. If true, such contrast in conductivity would lead to higher ice temperatures and dielectric constants near the UPLD-LPLD unconformity. This would not generate a great deal of difference from our dielectric profile results. But in the presence of salts, such as the sulfate deposits observed in association with the LPLD by Mars Express [*Langevin et al.*, 2005a], the warmer ice could melt in small amounts. If this indeed happens, the behavior predicted by mixing deLoor and Tinga-Voss-Blossey formulas breaks down. *Herique et al.* [2002] measured the dielectric behavior of several mineral phases admixed with water ice between 77 K and 250 K and found a relatively complex dependence of both real and imaginary parts of dielectric constants on temperature, and they attributed the complexity to dispersion and ionic solutions, respectively (due to briny water films surrounding inclusion grains) at the lower and higher ends of the studied temperature range. The range in ε' and ε'' for ice-bearing dunite reported by *Herique et al.* [2002], for example, is ~4.5 to 13 and $\sim 10^{-3}$ to 2, respectively. Although the range adopted for silicate inclusions in our study covers the values of *Heggy et al.* [2001] and *Herique et al.* [2002] and should provide a good first order estimate of propagation depth and layering detection, thermal models with greater fidelity to Mars (i.e., incorporating ice impurities and more realistic stratigra-

phies) may alter the results to some degree and should be attempted when interpreting data returned from radar sounders orbiting Mars.

6. Conclusion

[47] The mapping of layering within the Martian PLD by SHARAD is feasible down to a resolution of $\sim$ 20 m and for plausible dust content distributions estimated from ice albedo and the radiative transfer model of *Kieffer* [1990], as long as minimum dust fractions amount to more than 10^{-3}. This fraction value is quite possibly a lower bound on the actual occurrence of dust. Recent estimates based on infrared remote sensing set an upper bound to inclusion fractions on the order of a few percent near the surface, which would imply dust fractions >10% deep in the UPLD as albedo is lower at depth. Deep penetration of the radar signal and mapping of the PLD unconformity, or the direct contact between the ice-rich units and the crust, is likely if dust inclusion fractions are near the lower bound value for the range of inclusion dielectric constants used in this study. If reality lies near the upper bound limit of dust fraction, then substantial penetration and characterization of the entire PLD column is very unlikely in the case inclusions that are dielectrically strong. Signal attenuation is very efficient and occurs within several hundred meters if the dielectric constant of inclusions is similar to $\varepsilon_{incl} = 15 + i\ 1.5$. Small degrees of melting in the lower PLD, due to the interaction of ice and possible saline deposits, could also enhance dielectrically weak inclusions (by enclosing them in thin films of brine) to higher effective values that would prevent the detection of structures at deeper levels. Current thermal models of the cap, however, are too simplistic and their enhancement is mandatory in order to support the proper appraisal of the radar data. Finally, seasonal carbon dioxide frost may enhance subsurface reflections by 20 dB at best and facilitate the detection of subsurface reflectors. The Martian polar caps represent one of the best targets for radar sounding, and so it is imperative to understand their composition and physical state through better modeling and synergy with other remote sensing data sets.

[48] **Acknowledgments.** This work was carried out in part at the Lunar and Planetary Institute, which is run by the Universities Space Research Association under NASA Cooperative Agreement NCC5-679. The authors were also supported in part by contracts to Washington University from the Mars Reconnaissance Orbiter project of the Jet Propulsion Laboratory, California Institute of Technology. The authors would like to thank John Holt for his thorough review of the manuscript, which led to an enhanced discussion of the model and results. DCN would also like to thank the USGS Astrogeology staff for a helpful ISIS/GIS online tutorial and discussion. Lunar and Planetary Institute Contribution 1305.

References

Bandfield, J. L. (2002), Global mineral distributions on Mars, *J. Geophys. Res.*, *107*(E6), 5042, doi:10.1029/2001JE001510.

Bass, D. S., and D. A. Paige (2000), Variability of Mars' north polar water ice cap, *Icarus*, *144*, 397–409.

Benson, J. L., and B. A. Cantor (2005), Yearly comparisons of the Martian polar caps: 1999–2003 Mars Orbiter Camera observations, *Icarus*, *174*, 513–523.

Boynton, W. V., et al. (2002), Distribution of hydrogen in the near surface of Mars: Evidence for subsurface ice deposits, *Science*, *297*, 81–85.

Brückner, J., G. Dreibus, R. Rieder, and H. Wänke (2003), Refined data of Alpha Proton X-ray Spectrometer analyses of soils and rocks at the Mars Pathfinder site: Implications for surface chemistry, *J. Geophys. Res.*, *108*(E12), 8094, doi:10.1029/2003JE002060.

Byrne, S., and A. P. Ingersoll (2003), A sublimation model for Martian south polar ice features, *Science*, *299*, 1051–1053.

Byrne, S., and B. C. Murray (2002), North polar stratigraphy and the paleoerg of Mars, *J. Geophys. Res.*, *107*(E6), 5044, doi:10.1029/2001JE001615.

Chyba, C. F., et al. (1998), Radar detectability of a subsurface ocean on Europa, *Icarus*, *134*, 292–302.

Davidson, D. W. (1973), Clathrate hydrates, in *Water: A Comprehensive Treatise*, edited by F. Franks, pp. 115–234, Springer, New York.

Edgett, K. S., et al. (2003), Mars landscape evolution: Influence of stratigraphy on geomorphology in the north polar region, *Geomorphology*, *52*, 289–297.

Fishbaugh, K. E., and J. W. Head III (2005), Origin and characteristics of the Mars north polar basal unit and implications for polar geologic history, *Icarus*, *174*, 444–474.

Frey, H. V., J. H. Roark, K. M. Shockey, E. L. Frey, and S. E. H. Sakimoto (2002), Ancient lowlands on Mars, *Geophys. Res. Lett.*, *29*(10), 1384, doi:10.1029/2001GL013832.

Gellert, R., et al. (2004), Chemistry of rocks and soils in Gusev crater from the alpha particle x-ray spectrometer, *Science*, *305*, 829–832.

Hale, A. S., et al. (2005), Monitoring the perennial Martian northern polar cap with MGS MOC, *Icarus*, *174*, 502–512.

Heggy, E., et al. (2001), On water detection in the Martian subsurface using sounding radar, *Icarus*, *154*, 244–257.

Herique, A., et al. (2002), Dielectric properties of comet analog refractory materials, *Planet. Space Sci.*, *50*, 857–863.

Herkenhoff, K. E., and B. C. Murray (1990), Color and albedo of the south polar layered deposits on Mars, *J. Geophys. Res.*, *95*(B2), 1343–1358.

Herkenhoff, K. E., et al. (2004), Evidence from Opportunity's Microscopic Imager for Water on Meridiani Planum, *Science*, *306*, 1727–1730.

James, P. B., and B. A. Cantor (2001), Martian north polar cap recession: 2000 Mars Orbiter Camera observations, *Icarus*, *154*, 131–144.

James, P. B., et al. (1992), The seasonal cycle of carbon dioxide on Mars, in *Mars*, edited by H. H. Kieffer et al., pp. 934–968, Univ. of Ariz. Press, Tucson.

Kieffer, H. H. (1990), H_2O grain size and the amount of dust in Mars' residual north polar cap, *J. Geophys. Res.*, *95*(B2), 1481–1493.

Kieffer, H. H., and T. N. Titus (2001), TES mapping of Mars' north seasonal cap, *Icarus*, *154*, 162–180.

Kolb, E. J., and K. L. Tanaka (2001), Geologic history of the polar regions of Mars based on Mars Global Surveyor Data, II. Amazonian Period, *Icarus*, *154*, 22–39.

Langevin, Y., et al. (2005a), Sulfates in the north polar region of Mars detected by OMEGA/Mars Express, *Science*, *307*, 1584–1586.

Langevin, Y., et al. (2005b), Summer evolution of the north polar cap of Mars as observed by OMEGA/Mars Express, *Science*, *307*, 1581–1584.

Larsen, J., and D. Dahl-Jensen (2000), Interior temperatures of the northern polar cap on Mars, *Icarus*, *144*(2), 456–462.

Laskar, J., et al. (2002), Orbital forcing of the Martian polar layered deposits, *Nature*, *419*, 375–377.

Leighton, R. B., and B. C. Murray (1966), Behavior of carbon dioxide and other volatiles on Mars, *Science*, *153*, 136–144.

Lodders, K. (1998), A survey of shergottite, nakhlite, and chassigny meteorites whole-rock compositions, *Meteorit. Planet. Sci.*, *33*, A183–A190.

Malin, M. C., and K. S. Edgett (2001), Mars Global Surveyor Mars Orbiter Camera: Interplanetary cruise through primary mission, *J. Geophys. Res.*, *106*(E10), 23,429–23,570.

Matzler, C. (1998), Microwave properties of ice and snow, in *Solar System Ices*, edited by B. Schmitt et al., pp. 241–257, Springer, New York.

Mellon, M. T. (1996), Limits on the CO_2 content of the Martian polar deposits, *Icarus*, *124*, 268–279.

Milkovich, S. M., and J. W. Head III (2005), North polar cap of Mars: Polar layered deposit characterization and identification of a fundamental climate signal, *J. Geophys. Res.*, *110*, E01005, doi:10.1029/2004JE002349.

Mitrofanov, I. G., et al. (2003), CO_2 snow depth and subsurface water-ice abundance in the northern hemisphere of Mars, *Science*, *300*, 2081–2084.

Moore, H. J., et al. (1999), Soil-like deposits observed by Sojourner, the Pathfinder rover, *J. Geophys. Res.*, *104*, 8729–8746.

Olhoeft, G. R., and D. W. Strangway (1975), Dielectric properties of the first 100 meters of the Moon, *Earth Planet. Sci. Lett.*, *24*, 394–404.

Pettinelli, E., G. Vannaroni, A. Cereti, F. Paolucci, G. Della Monica, M. Storini, and F. Bella (2003), Frequency and time domain permittivity measurements on solid CO_2 and solid CO_2–soil mixtures as Martian soil simulants, *J. Geophys. Res.*, *108*(E4), 8029, doi:10.1029/2002JE001869.

Pettinelli, E., G. Vannaroni, A. Cereti, A. R. Pisani, F. Paolucci, D. Del Vento, D. Dolfi, S. Riccioli, and F. Bella (2005), Laboratory investiga-

tions into the electromagnetic properties of magnetite/silica mixtures as Martian soil simulants, *J. Geophys. Res.*, *110*, E04013, doi:10.1029/2004JE002375.

Picardi, G., et al. (2004), Performance and surface scattering models for the Mars Advanced Radar for Subsurface and Ionospheric Sounding (MARSIS), *Planet. Space Sci.*, *52*, 149–156.

Picardi, G., et al. (2005), Radar soundings of the subsurface of Mars, *Science*, *310*, 1925–1928.

Rieder, R., et al. (1997), The chemical composition of Martian soils and rocks returned by the mobile alpha proton x-ray spectrometer: Preliminary results from the x-ray mode, *Science*, *278*, 1771–1774.

Ruff, S. W., and P. R. Christensen (2002), Bright and dark regions on Mars: Particle size and mineralogical characteristics based on Thermal Emission Spectrometer data, *J. Geophys. Res.*, *107*(E12), 5127, doi:10.1029/2001JE001580.

Seu, R., et al. (2004), SHARAD: The MRO 2005 shallow radar, *Planet. Space Sci.*, *52*, 157–166, doi:10.1016/j.pss.2003.08.024.

Smith, D. E., et al. (2001), Seasonal variations of snow depth on Mars, *Science*, *294*, 2141–2146.

Soderblom, L. A., et al. (2004), Soils of Eagle crater and Meridiani Planum at the Opportunity rover landing site, *Science*, *306*, 1723–1726.

Thomas, P., et al. (1992), Polar deposits of Mars, in *Mars*, edited by H. H. Kieffer et al., pp. 767–795, Univ. of Ariz. Press, Tucson.

Thomas, P. C., et al. (2000), North-south geological differences between the residual polar caps on Mars, *Nature*, *404*, 161–164.

Titus, T. N., et al. (2003), Exposed water ice discovered near the south pole of Mars, *Science*, *299*, 1048–1051.

Ulaby, F. T., et al. (1986), *Microwave Remote Sensing: Active and Passive*, Artech House, Norwood, Mass.

Wait, J. R. (1970), *Electromagnetic Waves on Stratified Media*, Elsevier, New York.

Ward, S. H., et al. (1968), Electromagnetic reflection from a plane-layered lunar model, *J. Geophys. Res.*, *73*(4), 1355–1372.

Williams, K. K., and R. Greeley (2004), Measurements of dielectric loss factors due to a Martian dust analog, *J. Geophys. Res.*, *109*, E10006, doi:10.1029/2002JE001957.

D. C. Nunes, Lunar and Planetary Institute, 3600 Bay Area Boulevard, Houston, TX 77058, USA. (nunes@lpi.usra.edu)

R. J. Phillips, Department of Earth and Planetary Sciences, Washington University, Campus Box 1169, 1 Brookings Drive, St. Louis, MO 63130, USA.